# Tailoring Growth Kinetics toward a Size-Dependent Work Function of Ge Nanocrystals Synthesized by Inert Gas Condensation

Zhu, Xiaotian; Xing, Lijuan; Ten Brink, Gert H.; Kooi, Bart J.; Palasantzas, George

*Published in:*
Journal of Physical Chemistry C

*DOI:*
10.1021/acs.jpcc.1c02079



*Publication date:*
2021

THE JOURNAL OF PHYSICAL CHEMISTRY C
A JOURNAL OF THE AMERICAN CHEMICAL SOCIETY

pubs.acs.org/JPCC

Article

# Tailoring Growth Kinetics toward a Size-Dependent Work Function of Ge Nanocrystals Synthesized by Inert Gas Condensation

Xiaotian Zhu, Lijuan Xing, Gert H. ten Brink, Bart J. Kooi, and George Palasantzas*

Cite This: *J. Phys. Chem. C* 2021, 125, 12870−12879

Read Online

ACCESS | Metrics & More | Article Recommendations | Supporting Information

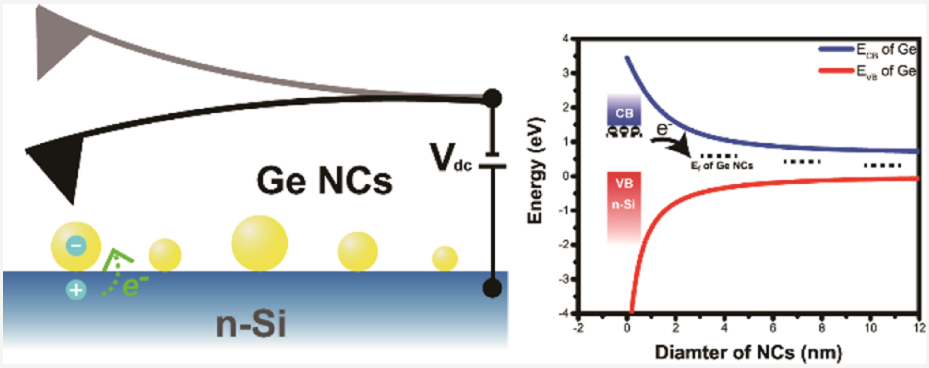


**ABSTRACT:** Understanding the size-dependent electronic properties of germanium nanocrystals (Ge NCs) is of fundamental importance for improving the efficiency of optoelectronic devices based on such NCs. Here, Ge NCs with a tunable size were synthesized by magnetron-sputtering cluster-beam deposition, where the size of the as-deposited Ge NCs can be finely controlled between 6 and 36 nm by helium gas flow rates and variable magnetic field configurations above the target surface. Because the size of the as-deposited Ge NCs highly depends on the nucleation process inside the plasma region, a detailed comparison between these two process parameters on the size control was formulated from the perspective of the growth kinetic mechanism. Furthermore, the local surface potential of different-sized Ge NCs deposited on n-type silicon substrates was measured by Kelvin probe force microscopy. The surface potential fluctuation of n-type Si covered by Ge NCs shows a strong size-dependent relationship with the size of the Ge NCs, whereas the surface potential fluctuation increases when their size reduced. Because the surface potential fluctuation between the intrinsic Ge NCs and the n-type silicon substrate tends to get smaller as the NCs' size decreases due to the quantum confinement effect, the number of charges transferred between the electronic bands will reduce as the size of Ge NCs decreases. The latter exactly explains the observed experimental results. Therefore, this work offers a perspective to understand the behavior of charge transfer, which plays an important role in the performance of optoelectronic devices.

## 1. INTRODUCTION

Semiconductor nanocrystals (NCs) have been the subject of relentless research due to their size-dependent physical properties, which make them potential candidates for electronic and optoelectronic applications.[1,2] Based on the quantum confinement theory, when the radius of NCs is scaled down below their Bohr exciton radius, the band gap energy of semiconductor NCs can be tuned by varying their size.[3] Although the binary NC systems that are made up of group III−V or II−VI elements have been well developed, the group IV semiconductor NCs also remain of strong interest that continue to inspire intense research. One main interest that arises for group IV NCs, especially for Si NCs, stems from the fact that they are compatible with the existing microelectronic industry and as a result reduce the cost of technological integration. Moreover, because group IV NCs exclude the use of toxic heavy-metal elements, for example, Cd and Pd, they are deemed suitable for further biological applications.[4,5] Among the group IV NCs, germanium (Ge) NCs are highly promising due to their relatively larger Bohr exciton radius[6] (∼24 nm) and absorption coefficient[7] (∼2 × $10^5$ $cm^{-1}$ at 2 eV), which make them attractive, especially for optoelectronic applications, such as light-emitting devices[8] and solar cells.[9]

Furthermore, in many microelectronic applications, the exchange of charge at the interface of the device is one of the essential processes for further development.[10,11] In the case of a quantum dot (QD)-sensitized solar cell, the process of carrier dissociation and charge transport at the interface between the

**Received:** March 8, 2021
**Revised:** May 24, 2021
**Published:** June 4, 2021

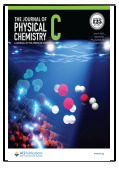







https://doi.org/10.1021/acs.jpcc.1c02079
*J. Phys. Chem. C* 2021, 125, 12870−12879

QD and the carrier transportation layer is crucial for the overall efficiency of the device.[12,13] Hence, improving the efficiency of such devices strongly depends on the level of understanding of the relationship between the nanostructure and its electronic properties. Therefore, the work function of nanoobjects is an important parameter for devices because it is relevant for the barrier height that affects the carrier mobility.[14] However, when the bulk materials are reduced to nanometer-sized objects such as NCs, the investigation of the local electronic properties of these nanoobjects becomes increasingly challenging.[15] In addition, due to the inevitable imperfections during the fabrication of NCs, the electronic properties of NCs are also affected by defects and impurities.[16]

Although the surface potential or work function can be characterized by conventional spectroscopic techniques such as photoelectron spectroscopy (PES),[17] due to the limitations in the spatial resolution of spectroscopic methods, the properties of the individual nanostructure cannot be resolved. Nevertheless, in recent years, scanning probe techniques, such as Kelvin probe force microscopy (KPFM) and/or electrostatic force microscopy (EFM), have been widely used to characterize the electronic properties of semiconductor NCs[13,18] and biological materials.[19] Even though scanning tunneling microscopy is a prevalent method for studying the electronic properties of NCs,[20−22] it is restricted to conductive materials (i.e., metal or highly conductive semiconductor). Moreover, the presence of tip-induced band bending can result in the inaccurate interpretation of results. On the other hand, KPFM measurements can overcome these limitations. Because the latter is an atomic force microscopy (AFM)-based technique, it is appropriate to investigate the electrical properties of various systems such as metallic nanoparticles,[23,24] semiconductor NCs,[25,26] and organic materials[27] from the meso- to nanoscopic levels.[10,17] Currently, several studies have demonstrated that KPFM can be applied to characterize the electrostatic properties of semiconductor NCs,[28] involving the size-dependent work function of InAs NCs grown on GaAs[14] and the charge states of Si NCs.[29] However, most of the studies investigated mainly homogeneous thin films of colloidal NCs, from which it is hard to access information on individual NCs, and they also cannot exclude the side effects of ligands.[13,16]

Therefore, so far, only limited research has been focused on the investigation of electrostatic properties of Ge QDs grown by molecular beam epitaxy, which shows only one-dimensional confinement below the Bohr exciton radius of Ge.[30,31] Hence, gas-phase Ge NCs represent a desirable three-dimensional (3D) model that enables the study of the properties of free-standing Ge NCs forming 3D confined QDs. In this regard, the routes for synthesizing Ge NCs can be divided into solution-phase methods, such as the sol−gel process,[32,33] microwave-assisted reduction,[34,35] thermal decomposition,[36,37] and gas-phase methods, including nonthermal plasma,[38] and cluster-beam deposition.[39,40] The several advantages of the gas-phase method compared to the solution-phase method for synthesizing Ge NCs include environmentally friendly routes, easy size control, and ligand-free NCs. The elimination of the side-effects of surface ligands enables the investigation of the electrostatic properties of individual Ge NCs.

Therefore, in this work, the gas-phase Ge NCs were synthesized by a high-pressure magnetron-sputtering cluster source, and they were used as a model candidate to investigate the size-dependent electrical properties of free-standing NCs by KPFM. Initially, the size of as-deposited Ge NCs can be tuned by changing the helium gas flow rate and placing backing plates behind the target during the deposition.[39] The effect of these two parameters on the size and crystallinity of the NCs was analyzed and discussed from the growth kinetic mechanism point of view. Subsequently, the work function of Ge NCs deposited with different sizes on n-type Si substrates was studied by KPFM, demonstrating a shift of the Fermi level as a function of the size of the NCs. The results obtained by KPFM can be well interpreted as a function of the size of the Ge NCs by the quantum confinement theory.

## 2. METHODS

**2.1. NC Synthesis.** The different-sized Ge NCs were directly deposited on Si substrates by a home-modified nanoparticle system Nanogen 50 obtained from Mantis Deposited Ltd. (www.mantisdeposited.com).[39] The Ge NCs were directly synthesized by high-pressure magnetron sputtering from a Ge target (50.8 mm diameter, 3 mm thickness, and purity of 99.99%) under Ar gas flow (99.9999%) and a 0.20 A discharge current. The main chamber, where the substrate was placed, was initially evacuated to a base pressure of $\sim 1 \times 10^{-8}$ mbar. The deposition yield can be monitored by a quartz crystal microbalance (QCM) placed next to the substrate holder. The average size of Ge NCs could be tuned from 36 to 20 nm by controlling the ratio of added helium (He) gas flow with respect to main sputtering gas (Ar), and without putting any backing plates. However, for smaller Ge NCs (<16 nm), various copper backing plates, with their thickness varying between 1.5 and 6 mm, were placed in-between the Ge target and the magnetron head, as well as the Ar flow rate was maintained at 20 sccm, to achieve the desired size tuning of the as-deposited NCs. The latter is achieved because one can adjust the magnetic field strength on the target surface where the sputtering takes place.[39]

**2.2. Transmission Electron Microscopy.** The morphology and crystalline structures of the Ge NCs deposited on carbon films were directly characterized after deposition using a transmission electron microscope (JEOL 2010) operated at 200 kV. High-resolution transmission electron microscopy (HRTEM) images were also recorded using a Thermo Fisher Scientific Themis Z S/TEM with a probe and an image corrector operating at 300 kV.

**2.3. Atomic and Kelvin Probe Force Microscopy.** The morphology and electrical properties of as-deposited Ge NCs were characterized using a Multimode 8 AFM system (Bruker, Santa Barbara, CA) under ambient conditions. The morphology of as-deposited Ge NCs was imaged in tapping mode using a sharp silicon tip (cantilever resonance frequency ∼ 325 kHz and spring constant 40 N/m). For the KPFM measurements, the samples were imaged in a lift mode, also known as amplitude-modulation KPFM (AM-KPFM), using a Pt-coated silicon tip (cantilever resonance frequency ∼ 75 kHz and spring constant ∼ 2.8 N/m). The typical radius of a coated tip is below 20 nm, and it has a similar size as the Ge NCs under investigation. In this case, because the local electrostatic interaction from the cantilever surface can be minimized in the lift mode, reasonable accurate results could be expected.[41,42] In the lift mode, during the first pass, the sample is scanned to obtain the topographical information. Subsequently, during the second pass, the cantilever is raised to a user-defined height, following the stored topography data, where the surface potential is measured. In order to minimize the error of the tip convolution that originates from the side-capacitance effect[43]



https://doi.org/10.1021/acs.jpcc.1c02079
J. Phys. Chem. C 2021, 125, 12870−12879

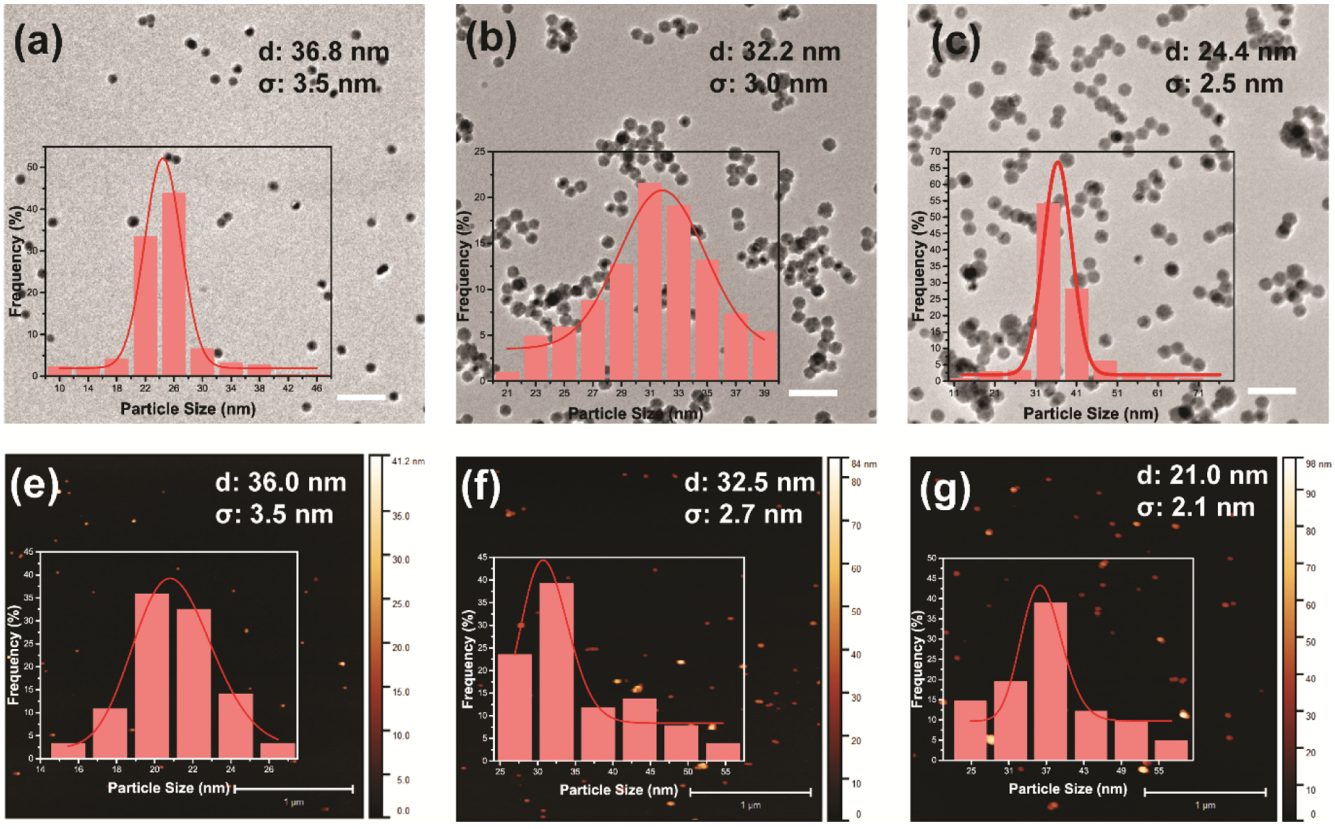


**Figure 1.** Size distribution analysis of the Ge NCs deposited by gas-phase condensation via tuning the Ar/He gas ratio: 30/0 sccm (left column); 20/10 (middle column); and 25/5 (right column). (a–c) Overview TEM images of three different-sized Ge NCs (scale bar is 100 nm) and (e–g) AFM height topography image of the Ge NCs measured in the tapping mode (scale bar is 1 $\mu$m). Inset: Size histograms of the Ge NCs with curves fitted to the Gaussian size distribution model.

and maintain a sufficient signal-to-noise ratio when the lift height is too high, as well as to avoid topography contributions due to van der Waals interactions at shorter ranges, several experiments at different lift heights were conducted. The result of the relationship between the measured ΔCPD and the lift height is shown in the Supporting Information (Figure S2), which indicates that 25 nm is an effective lift height for the KPFM measurements.

During the KPFM measurement, both a DC voltage $V_{dc}$ and an AC voltage $V_{ac}\sin(\omega t)$ were applied to the tip, as shown in Figure S6.[17] The $V_{dc}$ is adjusted to compensate for the electrostatic forces (by nullifying the first harmonic), and this is recorded as the contact potential difference (CPD) between the AFM tip and the sample. The latter is defined as

$$V_{CPD} = \frac{\Phi_{sample} - \Phi_{tip}}{e} \tag{1}$$

Furthermore, the surface potential fluctuation of n-type Si covered by Ge NCs is termed as ΔCPD for the Ge NCs. Also, the ΔCPD of the Ge NCs with respect to the substrate can be defined as

$$\Delta V_{CPD(NC/sub)} = \frac{\Phi_{sub} - \Phi_{tip}}{e} - \frac{\Phi_{NC} - \Phi_{tip}}{e} = \frac{(\Phi_{sub} - \Phi_{NC})}{e} \tag{2}$$

where the $\Phi_{sub}$ and $\Phi_{NC}$ are the work functions of the substrate and as-deposited Ge NCs, respectively. In practice, the tip–sample can be considered as a capacitor, and the electrostatic force of the tip–sample is expressed as

$$F_{es} = -\frac{1}{2}\frac{dC}{dz}[(V_{dc} - V_{CPD}) + V_{ac}\sin(\omega_{AC}t)]^2 \tag{3}$$

where the $dC/dz$ is the gradient of the capacitance between the tip and the sample surface. $F_{es}$ can be divided into three components, wherein the first harmonic component of $F_{es}$, $F_{\omega}$, depends on the $V_{CPD}$ as

$$F_{\omega} = -\frac{dC}{dz}(V_{dc} - V_{CPD})V_{ac}\sin(\omega_{AC}t) \tag{4}$$

Therefore, the feedback loop is employed to nullify $F_{\omega}$ by adjusting $V_{dc}$ and measuring the $V_{CPD}$ between the tip and the sample.

## 3. RESULTS AND DISCUSSION

Overview TEM images of different-sized as-deposited Ge NCs are shown in Figure 1a–c, which also showcase the dependence of the average size evolution on the ratio of the He/Ar gas mixture for a constant total gas flow rate. The insets of Figure 1a–c show the corresponding statistical analysis of the size distribution with both the mean size and standard deviation, indicating relatively monodisperse size distributions. These results demonstrate that the size of Ge NCs decreases with increasing the rate of the He gas flow. The mean sizes of as-deposited Ge NCs, as derived from the TEM images, are 36.8 ± 3.5, 32.2 ± 3.0, and 24.4 ± 2.5 nm for 0 (Ar/He: 30/0), 10 (Ar/He: 20/10), and 25 (Ar/He: 5/25) sccm gas flow


https://doi.org/10.1021/acs.jpcc.1c02079
J. Phys. Chem. C 2021, 125, 12870–12879

rates, respectively. Moreover, the different-sized Ge NCs were simultaneously deposited on n-doped Si substrates, where their size was characterized by AFM (Figure 1d–f). The resulting mean sizes calculated by the AFM topography images are 36.0 ± 3.5, 32.5 ± 2.7, and 21.0 ± 2.1 nm, respectively. Table 1 shows a comparison of the results obtained after analysis of the size distributions from both the TEM and AFM images demonstrating a good agreement between both techniques.

**Table 1. Comparison of the Resulting Mean Size of Ge NCs, as Obtained from TEM and AFM Images, Using Different He Gas Flow Rates (for a Constant Total He + Ar Gas Flow Rate) during Ge NC Production**

| | helium gas flow rate (sccm) | | |
|---|---|---|---|
| | 0 | 10 | 25 |
| $D_{TEM}$ (nm) | 36.5 ± 3.5 | 32.2 ± 3.0 | 24.4 ± 2.5 |
| $D_{AFM}$ (nm) | 36.8 ± 3.5 | 32.2 ± 2.7 | 21.0 ± 2.1 |

The explanation for the influence of the He gas flow rate on the size distribution of as-deposited Ge NCs is that the drift velocity of NCs increases by increasing the He gas rate, which leads to a decrease of the residence time of Ge nanoclusters in the growth area.[44,45] As extensively described in the literature,[46,47] the free gas-phase Ge atoms are generated by the impact of accelerated $Ar^+$ ions on the target surface resulting in plasma confinement on the target surface. Afterward, the formation process of nanoparticles can be divided into three regimes. In the initial stage, a three-body collision between sputtered Ge atoms and cold Ar atoms induces the formation of unstable nuclei seeds (e.g., dimers), where Ar atoms are more efficient than the He atoms for the formation of the dimer bond. Subsequently, the dimers serve as the nuclei seeds for more Ge atoms in the supersaturated state landing on their surface. The latter contributes to the rapid growth of stable nanoclusters. Finally, the collision between nanoclusters leads to further growth of nanoparticles. Hence, the tunable size of as-deposited Ge nanoparticles can be achieved by interrupting the condensation process at a specific stage. During the condensation process, the primary role of He gas is to serve as the transport gas for nanoclusters, which can entrap the clusters more effectively in the gas streamlines reducing the residence time of clusters in the aggregation volume.[48] However, as stated above, due to the comparatively lower efficiency of He for dimer formation than Ar, as shown in Figure S1, with an increase in the supply rate of He gas, the deposition yield of Ge NCs will decrease. Because the function of Ar gas is not only to serve as the carrier gas for drifting nanoparticles to the exit of the source but also as the sputtering gas for facilitating the nucleation process, there is a nonobvious effect of the Ar flow rate on the size of the synthesized nanoparticles.[48]

Furthermore, as in our previous report,[39] the size distribution of Ge NCs can also be tuned by adjusting the magnetic field strength above the target surface. This is achieved by placing copper backing plates with different thicknesses behind the target. Figure 2 shows an overview of the tunable size range of as-deposited Ge NCs, from ~36 to ~7 nm, by adjusting the two relatively effective parameters (He/Ar gas mixture and magnetic field strength) for cluster beam deposition. In general, the size-control mechanism of the two methods is similar, which is by the modification of the nucleation process of nanoparticle growth that takes place

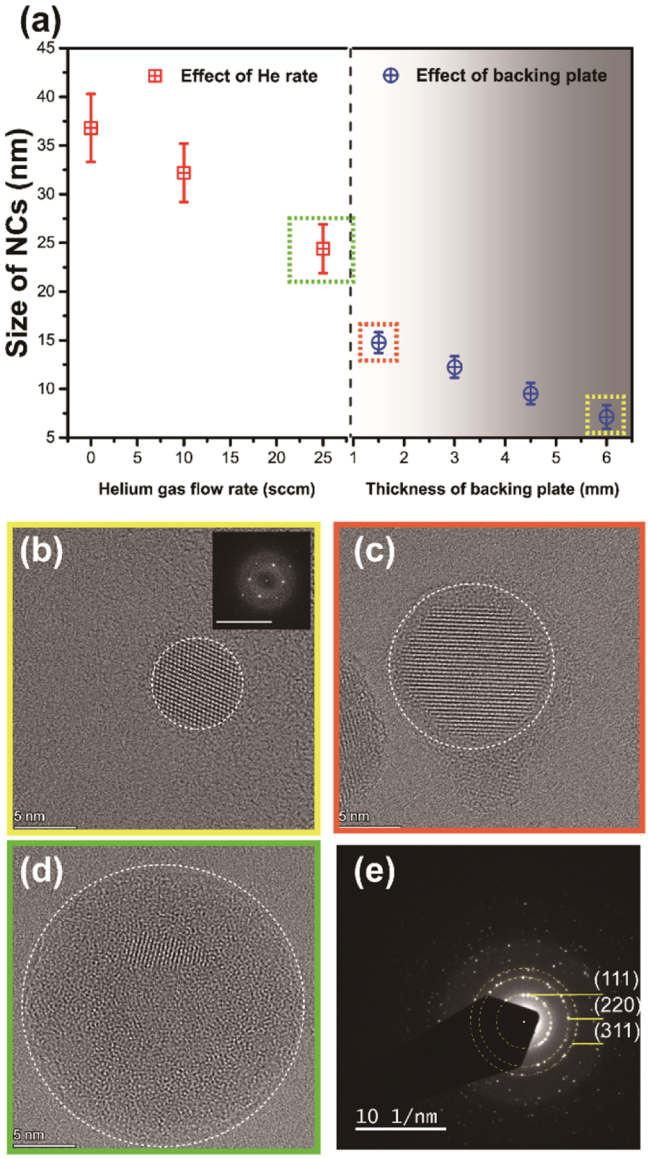


**Figure 2.** (a) Average diameter of the Ge NCs synthesized by tuning the He gas flow rate (left panel) and the thickness of the backing plate (right panel), individually. The size distribution analysis is based on TEM images. (b–d) HRTEM images of Ge NCs with different sizes as obtained from different experimental conditions marked in (a). (e) SAED images of as-deposited Ge NCs.

within the plasma region. Unlike the effect of helium gas flow, a stronger magnetic field induces an increased ionization of gas atoms ($Ar^+$) and reduces the diffusion rate of Ge atoms away from the source resulting in bigger Ge nanoparticles.[49,50] Note that there is a clear lower limit for the tunable size range for the as-deposited Ge NCs by regulating the individual parameters. For instance, the size of Ge NCs cannot be further decreased when the Ar/He ratio exceeds 25/5 sccm because dimers cannot be formed by sputtering in pure He gas. Similarly, when the magnetic field above the target surface is too weak, by inserting a relatively thicker backing plate, then achieving a confinement region with stable plasma is extremely challenging and the nuclei "seeds" cannot be formed in the plasma region.

Certainly, the smaller size of Ge nanoparticles can be achieved by integrating these two approaches by both increasing the He gas rate and using copper backing plates.


https://doi.org/10.1021/acs.jpcc.1c02079
J. Phys. Chem. C 2021, 125, 12870–12879

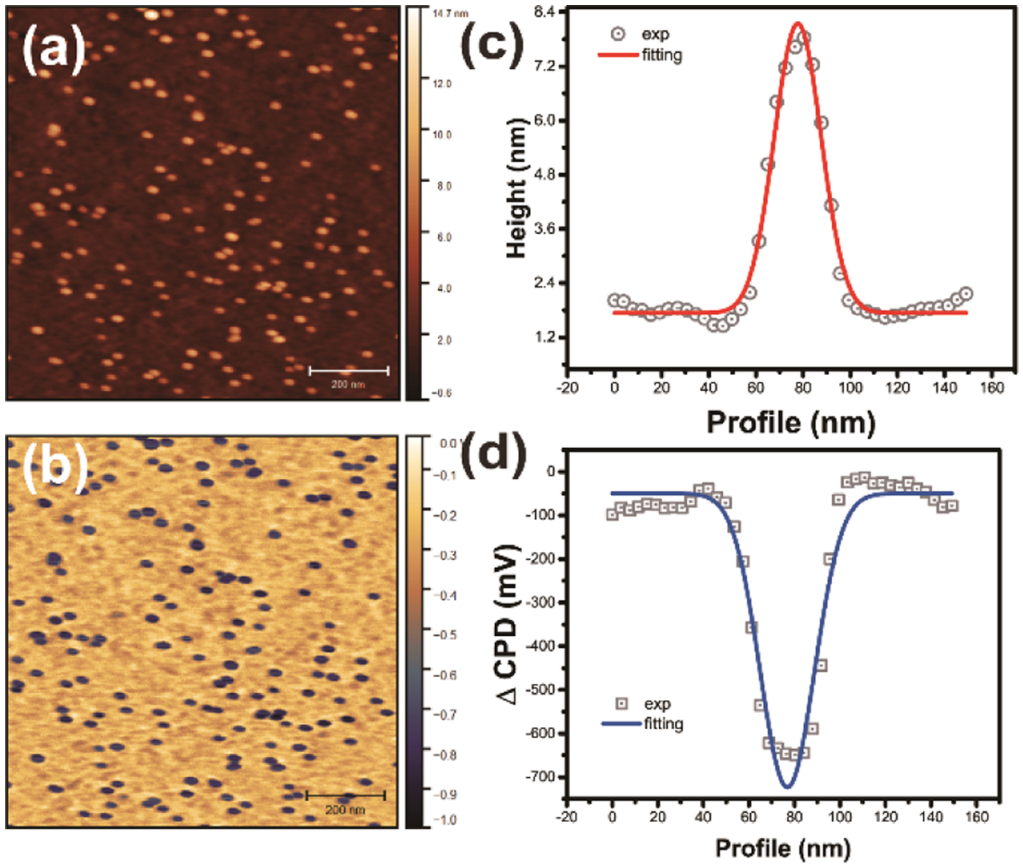


**Figure 3.** Determination of the height and ΔCPD for individual Ge NCs. (a) AFM image and the corresponding ΔCPD map (b) of the Ge NCs deposited on an n-type Si substrate. Example cross-section (c) and surface potential (d) profile of the lines marked in (a,b).

Nevertheless, in this scenario, the as-deposited Ge nanoparticles tend to appear to be in an amorphous state. Because the magnetic field projection on the Ge target decreases by placing a thicker backing plate, the accelerating path of the ionized gas atom will be shortened leading to less kinetic energy for the atoms in the plasma. As previously reported, the lower kinetic energy induces the formation of amorphous $Ge_2Sb_2Te_5$ nanoparticles.[51] On the other hand, in a previous work for the deposition of Si nanoparticles, it was indicated that a critical ratio of the number density of the Si and Ar atoms ($\rho_{Si}/\rho_{Ar}$) is essential for heating over the crystallization temperature during the condensation process.[44]

Furthermore, the crystalline structure of as-deposited Ge NCs with different sizes was characterized by HRTEM and selected area electron diffraction (SAED). As shown in Figure 2b–d, the HRTEM images of Ge NCs deposited by three different conditions, which are marked in Figure 2a, indicate that Ge NCs of all sizes are crystalline. Specifically, Figure 2b shows the typical single crystalline Ge NCs, here, for example, oriented along the [113] zone axis. Consequently, the interplanar d-spacings of the NC calculated from the fast Fourier transform, as shown in the inset of Figure 2b, are 0.326, 0.283, and 0.202 nm corresponding to the (111), (200), and (220) crystal planes of Ge. In addition, the SAED pattern in Figure 2e reveals the {111}, {220}, and {311} planes, which demonstrate that the as-deposited Ge NCs have the diamond cubic ($Fd\bar{3}m$) crystal structure. Although the majority of as-deposited NCs are single crystals, Ge NC with a partial amorphous state is also found in the HRTEM image in Figure 2d. The latter can lead to some deviation of the band structure.

In order to correlate the size of the NCs and electrical properties, Figure 3 shows typical AFM topography and the corresponding KPFM images of as-deposited Ge NCs on the n-doped Si substrate. Similarly, as shown in Figure 1, monodisperse Ge NCs of ∼7 nm height are observable in Figure 3a. Note that due to the convolution effect from the tip shape, the lateral dimensions of Ge NCs are inaccurate to obtain their sizes from the AFM images. Because the majority of as-deposited Ge NCs are monodisperse with a spherical-like shape in the TEM images (Figure 1), the NCs can be considered as nanodots in the AFM images. Thus, their diameter can be calculated by fitting a parabolic function to the peak of the height (Figure 3c). Similarly, the Ge NCs are also distinct in the KPFM images as dark spots (Figure 3b). The latter can be interpreted as the negative charging of the Ge NCs by the free carriers from the n-type Si substrate, even if the n-type Si substrate has a very thin native oxide layer. This is because for a very thin oxide layer, sufficient charge carrier transport can take place by tunneling through the $SiO_X$ layer, which has been proven by the experiment and simulation.[52] In addition, for the relatively thick oxide layer (2–5 nm), the defects inside the oxide layer can act as the pathway for carrier transportation.[52,53] Furthermore, Figure S3 in Supporting Information shows the result of KPFM measurements for Ge NCs deposited on a p-type Si substrate. In contrast to Figure 3b, where the Ge NCs manifest as dark features, the Ge NCs deposited on a p-type Si substrate manifest as bright features in the KPFM image. As the Fermi level of the p-type Si is lower than that of the Ge NCs, the positive carriers would be transferred from the p-type Si substrate to the Ge NCs. For


https://doi.org/10.1021/acs.jpcc.1c02079
J. Phys. Chem. C 2021, 125, 12870−12879

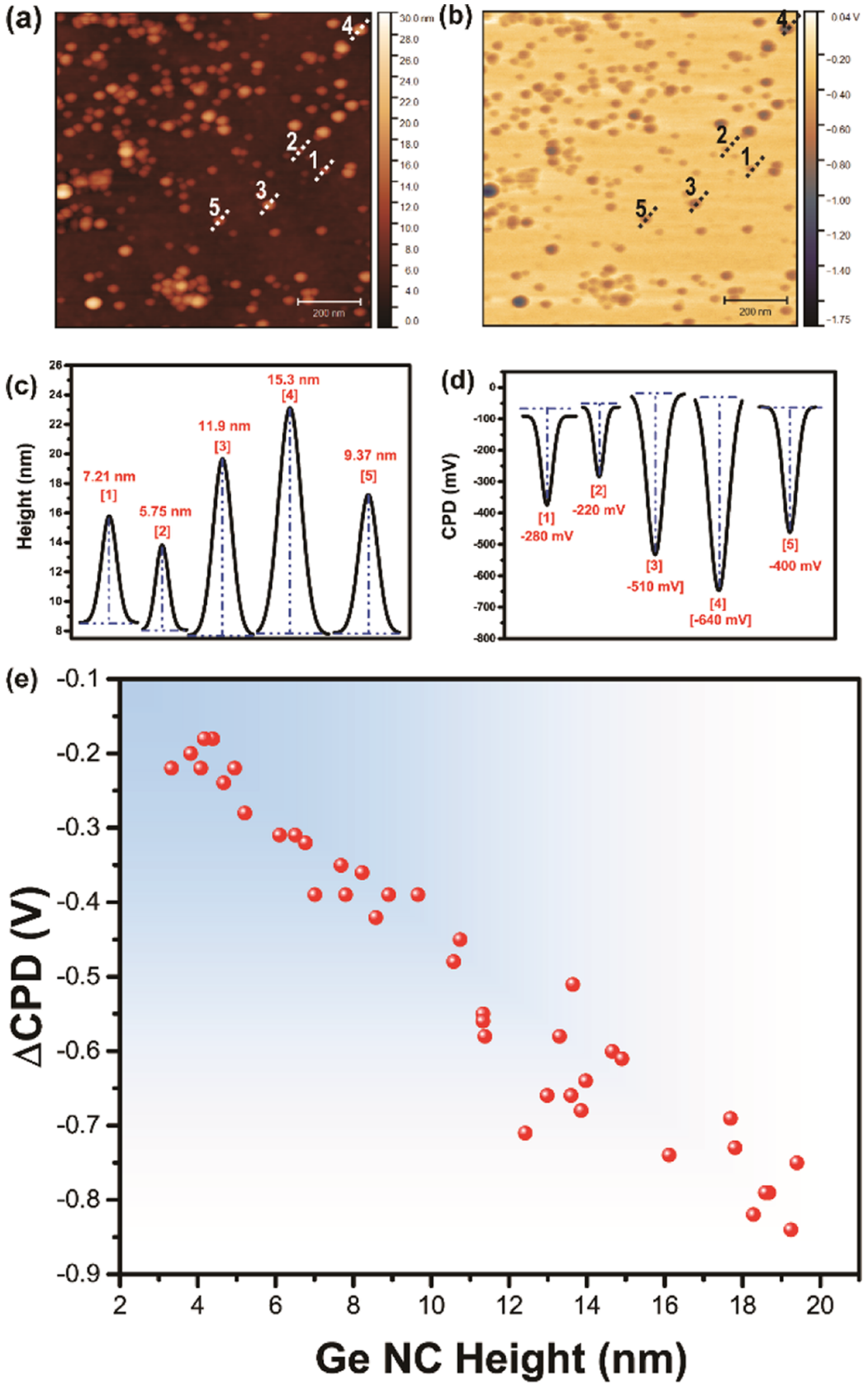


**Figure 4.** Simultaneously measured height topography (a) and the corresponding CPD image (b) of different-sized Ge NCs deposited on an n-type Si substrate. The scale bar is 200 nm. The fitted curves of the cross-section height profiles (c) and the corresponding CPD profiles (d) for five differently sized NCs marked in (a,b). (e) Dependence of the ΔCPD on the height of the NCs.



https://doi.org/10.1021/acs.jpcc.1c02079
J. Phys. Chem. C 2021, 125, 12870−12879

simplicity, the average CPD value of the n-type Si substrate was set to be zero in all results, and a similar approach was applied to measure the ΔCPD of the NCs with respect to the n-type Si substrate (Figure 3d).

The nominal size range to synthesize Ge NCs by adjusting the ratio of the Ar/He gas rate is roughly 16−30 nm, and this leads to some NCs with a size above the Bohr exciton radius of Ge (~24 nm). According to the quantum confinement effect, the band gap for this size of NCs cannot be tuned by varying their sizes. In this case, the Ge NCs below 16 nm in diameter, which were deposited by tuning the thickness of the backing plate, were considered for further KPFM measurements. In order to avoid interference from any discrepancy from the substrates and deposition, the Ge NCs with different sizes were deposited together onto single substrates. Figure 4a,b shows topographic and surface potential fluctuations of the n-type Si covered by Ge NCs, which are simultaneously measured by KPFM. In Figure 4c, a size variation between 5 and 16 nm is shown from the fitted results of the height profile for five typical Ge NCs. Accordingly, the corresponding ΔCPD fitted value of these NCs is shown in Figure 4d, which reveals a clear correlation with the size of Ge NCs. To investigate the observed size dependence, a systematic analysis of the ΔCPD values was performed on 30 differently sized NCs. As shown in Figure 4e, where the ΔCPD values of the NCs are plotted as a function of their height (which represents also the size of the NCs), the surface potential fluctuation increases with the decreasing size of the NCs.

The size dependence of the surface potential fluctuation for the Ge NCs can be explained by the quantum confinement theory. Recently, several similar phenomena have been shown by the quantum confinement theory for other systems such as Si NCs,[11] metal chalcogenide NCs,[13] and InAs NCs.[14,25] For instance, by fitting the X-ray photoelectron spectra into a calculated density of states model, it was demonstrated that the Fermi position of the PbS QD film depends on the QD size,[54] and similar results were also observed by KPFM measurements.[13] According to the quantum confinement theory, when the size of the Ge NCs is smaller or comparable to the Bohr exciton radius (~24 nm), the valence and conduction bands (VB/CBs) will shift to yield a wider band gap for the Ge NCs. Consequently, based on the $sp^3$ tight-binding calculation,[55,56] the energies of the VB maximum ($E_v$) and CB minimum ($E_c$) as a function of the Ge NCs' diameter can be described quantitatively as follows

$$E_v(d) = -\frac{15{,}143.8}{d^2 + 6.465d + 2.546}\text{meV} \quad (5)$$

$$E_c(d) = E_g(\text{bulk}) + \frac{11{,}863.7}{d^2 + 2.391d + 4.252}\text{meV} \quad (6)$$

where $d$ is the diameter (in nm) of the Ge NCs. The calculated trends of the energies for the VB maximum and the CB minimum from the tight-binding model are plotted in Figure 5. The latter demonstrates that the shift of the CB is, for the size range from 2 to 12 nm considered here, more pronounced than the shift of the VB. Because no doping elements were incorporated during the deposition process of Ge, the as-deposited Ge NCs can be considered as intrinsic semiconductors with their Fermi level close to the middle of the band gap. In this case, the Fermi level of the as-deposited Ge NCs will increase with the decrease of their diameter. Because the Fermi level of the n-type Si substrate is pinned, the amount

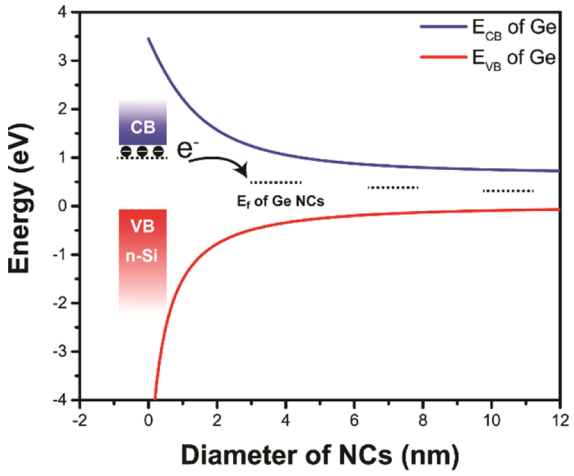


**Figure 5.** Predicted energy of the CB maximum and the VB minimum of Ge as a function of the diameter of the NCs based on the tight-binding model calculation. Inset: schematic diagram of the relative position of the Fermi level between the substrate and the Ge NCs with different sizes.

of the negative charge transfer from the substrate to the NCs depends on the variation of the Fermi levels for different sized Ge NCs. Consequently, as the energy diagram in Figure 5 illustrates, when the Ge NCs reduce in size, the Fermi level of the NCs is shifting increasingly closer to the Fermi level of the substrate, resulting in the decrease of the electrostatic energy of the ionized Ge NCs. In this case, the size-dependent effect manifests itself by increasing the surface potential fluctuation in KPFM images as the size of the Ge NCs decreases.

Furthermore, Figure S4 in Supporting Information, which shows the comparison between the normalized surface potential fluctuation for various sizes of Ge NCs and the theoretical model, demonstrates that the surface potential fluctuation for different-sized Ge NCs is comparable to the calculated results by the tight-binding model. However, the accurate extraction of the electrostatic potential for Ge NCs is affected by several factors including the side-capacitance and experimental conditions. For the lift mode KPFM, as the magnitude of the measured electrostatic potential is highly dependent on the geometry of the probe and lift height, the observed surface potential is a weighted average over all potentials from the localized sample surface. Despite the fact that the optimal experiments for the effects of lift height are carried out, and the results are shown in Figure S2, the side-capacitance effects cannot be fully excluded during the measurement, making the quantitative analysis for the electrostatic potential relatively difficult. Although the surface potential fluctuation can be interpreted as the charging of the Ge NC surface states by the free carriers from the Si substrate, the behavior of the charge carriers in semiconductors is influenced by the temperature, which causes an offset between the theoretical calculation and the experimental data.

Notably, the difference of the surface potential fluctuations for similar sized NCs originate from several deficiencies such as defects and surface oxidation during their deposition, which can be considered as the trap states for surface charges. Because the topography images of the Ge NCs were performed by tapping mode, these trap states from the deficiencies of Ge NCs could be continuously induced by the charges from the tip, and the surface itself could manifest the surface potential


https://doi.org/10.1021/acs.jpcc.1c02079
J. Phys. Chem. C 2021, 125, 12870−12879

fluctuations due to the local variation in the oxide charges. However, unlike the other semiconductor NCs such as Si NCs, based on the experimental observation (as it is shown in Figure S5), the partial Ge NCs remain in unoxidized states after 1 month of storage in air. Besides, doping for NCs would lead to a reduction of surface potential fluctuations due to the internal passivation mechanism, where the surface states could be occupied by donors of the NCs. In contrast to intrinsic NCs, where the net charges of the NCs generate a dipole perpendicular to the substrate,[57] the doping NCs would form a dipole with a random distribution inside the NCs.

## 4. CONCLUSIONS

In summary, tunable size Ge NCs were synthesized by magnetron-sputtering-based cluster-beam deposition, where the size of the as-deposited Ge NCs can be finely controlled by He gas flow rates and variable magnetic field configurations above the Ge target surface. Specifically, Ge NCs with a reduced size were obtained by an increase of the He gas flow rate during the deposition, which modifies the condensation process of the NCs. In addition, by comparing the effects of varying the He gas flow rates and the thickness of backing plates between the target and the magnetron head on the growth mechanism of the NCs, we discussed their influence on NC size and crystallinity. The analysis of HRTEM images and SAED patterns revealed that the Ge NCs have a diamond cubic crystal structure. Furthermore, the local electrical properties of different-sized free-standing Ge NCs were characterized by KPFM. The latter revealed a clear size-dependent relationship of the surface potential of the NCs. In particular, the surface potential fluctuation of n-type Si covered by Ge NCs increased linearly with a decrease of the NC height in good agreement with the quantum confinement effect. The measured size-dependent relationship can be explained as an increase in the number of charges transferred from the substrate to the NCs, which can be tuned by the size of Ge NCs. Based on the band energy calculation from the tight-binding theory, the energy of the Fermi level of the intrinsic Ge NCs will increase when their size reduces, which is consistent with the experimental results. The results obtained here are essential for pushing forward the understanding of charge exchange at the interfaces between semiconductor QDs and substrates that are of high importance to current and future nanoscale electronic devices.

## ■ ASSOCIATED CONTENT

### Supporting Information

The Supporting Information is available free of charge at https://pubs.acs.org/doi/10.1021/acs.jpcc.1c02079.

Relationship between measured CPD of NPs with the lift height for KPFM measurements, QCM data for different helium flow rates of deposition, topographic image and measured KPFM image of Ge NCs deposited on the p-type Si substrate, comparison between ΔCPD and theoretical model, TEM images of Ge NCs after 1 month storage in air, and the schematic setup of the KPFM measurement (PDF)

## ■ AUTHOR INFORMATION


### Corresponding Author

**George Palasantzas** − *Zernike Institute for Advanced Materials, University of Groningen, 9742 AG Groningen, The Netherlands;* orcid.org/0000-0002-5084-8769; Phone: +31 50 3634272; Email: g.palasantzas@rug.nl

### Authors

**Xiaotian Zhu** − *Zernike Institute for Advanced Materials, University of Groningen, 9742 AG Groningen, The Netherlands*

**Lijuan Xing** − *Department of Materials Science and Engineering, Southern University of Science and Technology, Shenzhen 518055, P. R. China*

**Gert H. ten Brink** − *Zernike Institute for Advanced Materials, University of Groningen, 9742 AG Groningen, The Netherlands*

**Bart J. Kooi** − *Zernike Institute for Advanced Materials, University of Groningen, 9742 AG Groningen, The Netherlands*

Complete contact information is available at: https://pubs.acs.org/10.1021/acs.jpcc.1c02079


### Notes

The authors declare no competing financial interest.

## ■ ACKNOWLEDGMENTS

X.Z. gratefully acknowledges the financial support from the China Scholarship Council (CSC, no. 201707040079).

## ■ REFERENCES


(1) Wang, Y.; Herron, N. Nanometer-Sized Semiconductor Clusters: Materials Synthesis, Quantum Size Effects, and Photophysical Properties. *J. Phys. Chem.* **1991**, *95*, 525−532.

(2) Zhang, Q.; Uchaker, E.; Candelaria, S. L.; Cao, G. Nanomaterials for Energy Conversion and Storage. *Chem. Soc. Rev.* **2013**, *42*, 3127−3171.

(3) Takagahara, T.; Takeda, K. Theory of the Quantum Confinement Effect on Excitons in Quantum Dots of Indirect-Gap Materials. *Phys. Rev. B: Condens. Matter Mater. Phys.* **1992**, *46*, 15578−15581.

(4) Prabakar, S.; Shiohara, A.; Hanada, S.; Fujioka, K.; Yamamoto, K.; Tilley, R. D. Size Controlled Synthesis of Germanium Nanocrystals by Hydride Reducing Agents and Their Biological Applications. *Chem. Mater.* **2010**, *22*, 482−486.

(5) Fan, J.; Chu, P. K. Group IV Nanoparticles: Synthesis, Properties, and Biological Applications. *Small* **2010**, *6*, 2080−2098.

(6) Carolan, D. Recent Advances in Germanium Nanocrystals: Synthesis, Optical Properties and Applications. *Prog. Mater. Sci.* **2017**, *90*, 128−158.

(7) Philipp, H. R.; Taft, E. A. Optical Constants of Germanium in the Region 1 to 10 Ev. *Phys. Rev.* **1959**, *113*, 1002−1005.

(8) Ruddy, D. A.; Johnson, J. C.; Smith, E. R.; Neale, N. R. Size and Bandgap Control in the Solution-Phase Synthesis of near-Infrared-Emitting Germanium Nanocrystals. *ACS Nano* **2010**, *4*, 7459−7466.

(9) Wheeler, L. M.; Nichols, A. W.; Chernomordik, B. D.; Anderson, N. C.; Beard, M. C.; Neale, N. R. All-Inorganic Germanium Nanocrystal Films by Cationic Ligand Exchange. *Nano Lett.* **2016**, *16*, 1949−1954.

(10) Liscio, A.; Palermo, V.; Samorí, P. Nanoscale Quantitative Measurement of the Potential of Charged Nanostructures by Electrostatic and Kelvin Probe Force Microscopy: Unraveling Electronic Processes in Complex Materials. *Acc. Chem. Res.* **2010**, *43*, 541−550.

(11) Borowik, Ł.; Kusiaku, K.; Deresmes, D.; Théron, D.; Diesinger, H.; Mélin, T.; Nguyen-Tran, T.; Roca I Cabarrocas, P. Mapping Charge Transfers between Quantum Levels Using Noncontact Atomic Force Microscopy. *Phys. Rev. B: Condens. Matter Mater. Phys.* **2010**, *82*, 073302.

(12) Mora-Seró, I.; Giménez, S.; Fabregat-Santiago, F.; Gómez, R.; Shen, Q.; Toyoda, T.; Bisquert, J. Recombination in Quantum Dot Sensitized Solar Cells. *Acc. Chem. Res.* **2009**, *42*, 1848−1857.
(13) Benetti, D.; Cui, D.; Zhao, H.; Rosei, F.; Vomiero, A. Direct Measurement of Electronic Band Structure in Single Quantum Dots of Metal Chalcogenide Composites. *Small* **2018**, *14*, 1801668−1801677.
(14) Yamauchi, T.; Tabuchi, M.; Nakamura, A. Size Dependence of the Work Function in InAs Quantum Dots on GaAs(001) as Studied by Kelvin Force Probe Microscopy. *Appl. Phys. Lett.* **2004**, *84*, 3834−3836.
(15) Tekiel, A.; Miyahara, Y.; Topple, J. M.; Grutter, P. Room-Temperature Single-Electron Charging Detected by Electrostatic Force Microscopy. *ACS Nano* **2013**, *7*, 4683−4690.
(16) Zhang, Y.; Zherebetskyy, D.; Bronstein, N. D.; Barja, S.; Lichtenstein, L.; Schuppisser, D.; Wang, L.-W.; Alivisatos, A. P.; Salmeron, M. Charge Percolation Pathways Guided by Defects in Quantum Dot Solids. *Nano Lett.* **2015**, *15*, 3249−3253.
(17) Melitz, W.; Shen, J.; Kummel, A. C.; Lee, S. Kelvin Probe Force Microscopy and Its Application. *Surf. Sci. Rep.* **2011**, *66*, 1−27.
(18) Mélin, T.; Deresmes, D.; Stiévenard, D. Charge Injection in Individual Silicon Nanoparticles Deposited on a Conductive Substrate. *Appl. Phys. Lett.* **2002**, *81*, 5054−5056.
(19) Clack, N. G.; Salaita, K.; Groves, J. T. Electrostatic Readout of DNA Microarrays with Charged Microspheres. *Nat. Biotechnol.* **2008**, *26*, 825−830.
(20) Banin, U.; Cao, Y.; Katz, D.; Millo, O. Identification of Atomic-like Electronic States in Indium Arsenide Nanocrystal Quantum Dots. *Nature* **1999**, *400*, 542−544.
(21) Millo, O.; Balberg, I.; Azulay, D.; Purkait, T. K.; Swarnakar, A. K.; Rivard, E.; Veinot, J. G. C. Direct Evaluation of the Quantum Confinement Effect in Single Isolated Ge Nanocrystals. *J. Phys. Chem. Lett.* **2015**, *6*, 3396−3402.
(22) Wolf, O.; Dasog, M.; Yang, Z.; Balberg, I.; Veinot, J. G. C.; Millo, O. Doping and Quantum Confinement Effects in Single Si Nanocrystals Observed by Scanning Tunneling Spectroscopy. *Nano Lett.* **2013**, *13*, 2516−2521.
(23) Dabera, G. D. M. R.; Walker, M.; Sanchez, A. M.; Pereira, H. J.; Beanland, R.; Hatton, R. A. Retarding Oxidation of Copper Nanoparticles without Electrical Isolation and the Size Dependence of Work Function. *Nat. Commun.* **2017**, *8*, 1894.
(24) Zhang, Y.; Pluchery, O.; Caillard, L.; Lamic-Humblot, A.-F.; Casale, S.; Chabal, Y. J.; Salmeron, M. Sensing the Charge State of Single Gold Nanoparticles via Work Function Measurements. *Nano Lett.* **2015**, *15*, 51−55.
(25) Biaye, M.; Amit, Y.; Gradkowski, K.; Turek, N.; Godey, S.; Makoudi, Y.; Deresmes, D.; Tadjine, A.; Delerue, C.; Banin, U.; et al. Doped Colloidal InAs Nanocrystals in the Single Ionized Dopant Limit. *J. Phys. Chem. C* **2019**, *123*, 14803−14812.
(26) Xu, J.; Xu, J.; Zhang, P.; Li, W.; Chen, K. Nanoscale Quantification of Charge Injection and Transportation Process in Si-Nanocrystal Based Sandwiched Structure. *Nanoscale* **2013**, *5*, 9971−9977.
(27) Fuchs, F.; Caffy, F.; Demadrille, R.; Mélin, T.; Grévin, B. High-Resolution Kelvin Probe Force Microscopy Imaging of Interface Dipoles and Photogenerated Charges in Organic Donor− Acceptor Photovoltaic Blends. *ACS Nano* **2016**, *10*, 739−746.
(28) Shusterman, S.; Raizman, A.; Sher, A.; Paltiel, Y.; Schwarzman, A.; Lepkifker, E.; Rosenwaks, Y. Nanoscale Mapping of Strain and Composition in Quantum Dots Using Kelvin Probe Force Microscopy. *Nano Lett.* **2007**, *7*, 2089−2093.
(29) Banerjee, S.; Salem, M. A.; Oda, S. Conducting-Tip Atomic Force Microscopy for Injection and Probing of Localized Charges in Silicon Nanocrystals. *Appl. Phys. Lett.* **2003**, *83*, 3788−3790.
(30) Singha, R. K.; Manna, S.; Bar, R.; Das, S.; Ray, S. K. Surface Potential, Charging and Local Current Transport of Individual Ge Quantum Dots Grown by Molecular Beam Epitaxy. *Appl. Surf. Sci.* **2017**, *407*, 418−426.
(31) Kondratenko, S. V.; Lysenko, V. S.; Kozyrev, Y. N.; Kratzer, M.; Storozhuk, D. P.; Iliash, S. A.; Czibula, C.; Teichert, C. Local Charge Trapping in Ge Nanoclustersdetected by Kelvin Probe Force Microscopy. *Appl. Surf. Sci.* **2016**, *389*, 783−789.
(32) Henderson, E. J.; Seino, M.; Puzzo, D. P.; Ozin, G. A. Colloidally Stable Germanium Nanocrystals for Photonic Applications. *ACS Nano* **2010**, *4*, 7683−7691.
(33) Henderson, E. J.; Hessel, C. M.; Veinot, J. G. C. Synthesis and Photoluminescent Properties of Size-Controlled Germanium Nanocrystals from Phenyl Trichlorogermane-Derived Polymers. *J. Am. Chem. Soc.* **2008**, *130*, 3624−3632.
(34) Muthuswamy, E.; Iskandar, A. S.; Amador, M. M.; Kauzlarich, S. M. Facile Synthesis of Germanium Nanoparticles with Size Control: Microwave versus Conventional Heating. *Chem. Mater.* **2013**, *25*, 1416−1422.
(35) Tabatabaei, K.; Holmes, A. L.; Newton, K. A.; Muthuswamy, E.; Sfadia, R.; Carter, S. A.; Kauzlarich, S. M. Halogen-Induced Crystallinity and Size Tuning of Microwave Synthesized Germanium Nanocrystals. *Chem. Mater.* **2019**, *31*, 7510−7521.
(36) Zaitseva, N.; Dai, Z. R.; Grant, C. D.; Harper, J.; Saw, C. Germanium Nanocrystals Synthesized in High-Boiling-Point Organic Solvents. *Chem. Mater.* **2007**, *19*, 5174−5178.
(37) Gerung, H.; Bunge, S. D.; Boyle, T. J.; Brinker, C. J.; Han, S. M. Anhydrous Solution Synthesis of Germanium Nanocrystals from the Germanium(II) Precursor Ge[N(SiMe3)2]2. *Chem. Commun.* **2005**, 1914−1916.
(38) Ahadi, A. M.; Hunter, K. I.; Kramer, N. J.; Strunskus, T.; Kersten, H.; Faupel, F.; Kortshagen, U. R. Controlled Synthesis of Germanium Nanoparticles by Nonthermal Plasmas. *Appl. Phys. Lett.* **2016**, *108*, 093105.
(39) Zhu, X.; ten Brink, G. H.; De Graaf, S.; Kooi, B. J.; Palasantzas, G. Gas-Phase Synthesis of Tunable-Size Germanium Nanocrystals by Inert Gas Condensation. *Chem. Mater.* **2020**, *32*, 1627−1635.
(40) Cardoso, J.; Marom, S.; Mayer, J.; Modi, R.; Podestà, A.; Xie, X.; van Huis, M. A.; Di Vece, M. Germanium Quantum Dot Grätzel-Type Solar Cell. *Phys. Status Solidi A* **2018**, *215*, 1800570.
(41) Zerweck, U.; Loppacher, C.; Otto, T.; Grafström, S.; Eng, L. M. Accuracy and Resolution Limits of Kelvin Probe Force Microscopy. *Phys. Rev. B: Condens. Matter Mater. Phys.* **2005**, *71*, 125424.
(42) Jacobs, H. O.; Leuchtmann, P.; Homan, O. J.; Stemmer, A. Resolution and Contrast in Kelvin Probe Force Microscopy. *J. Appl. Phys.* **1998**, *84*, 1168−1173.
(43) Borowik, Ł.; Kusiaku, K.; Théron, D.; Mélin, T. Calculating Kelvin Force Microscopy Signals from Static Force Fields. *Appl. Phys. Lett.* **2010**, *96*, 103119.
(44) Zhao, J.; Singh, V.; Grammatikopoulos, P.; Cassidy, C.; Aranishi, K.; Sowwan, M.; Nordlund, K.; Djurabekova, F. Crystallization of Silicon Nanoclusters with Inert Gas Temperature Control. *Phys. Rev. B: Condens. Matter Mater. Phys.* **2015**, *91*, 035419.
(45) Grammatikopoulos, P.; Steinhauer, S.; Vernieres, J.; Singh, V.; Sowwan, M. Nanoparticle Design by Gas-Phase Synthesis. *Adv. Phys. X* **2016**, *1*, 81−100.
(46) Huttel, Y. *Gas-Phase Synthesis of Nanoparticles*; John Wiley & Sons: New York, 2017.
(47) Haberland, H.; Mall, M.; Moseler, M.; Qiang, Y.; Reiners, T.; Thurner, Y. Filling of Micron-sized Contact Holes with Copper by Energetic Cluster Impact. *J. Vac. Sci. Technol., A* **1994**, *12*, 2925−2930.
(48) Khojasteh, M.; Kresin, V. V. Influence of Source Parameters on the Growth of Metal Nanoparticles by Sputter-Gas-Aggregation. *Appl. Nanosci.* **2017**, *7*, 875−883.
(49) Vernieres, J.; Steinhauer, S.; Zhao, J.; Chapelle, A.; Menini, P.; Dufour, N.; Diaz, R. E.; Nordlund, K.; Djurabekova, F.; Grammatikopoulos, P.; et al. Gas Phase Synthesis of Multifunctional Fe-Based Nanocubes. *Adv. Funct. Mater.* **2017**, *27*, 1605328.
(50) Palmer, R. E.; Cai, R.; Vernieres, J. Synthesis without Solvents: The Cluster (Nanoparticle) Beam Route to Catalysts and Sensors. *Acc. Chem. Res.* **2018**, *51*, 2296−2304.


https://doi.org/10.1021/acs.jpcc.1c02079
J. Phys. Chem. C 2021, 125, 12870−12879

(51) Chen, B.; Ten Brink, G. H.; Palasantzas, G.; Kooi, B. J. Size-Dependent and Tunable Crystallization of GeSbTe Phase-Change Nanoparticles. *Sci. Rep.* **2016**, *6*, 39546.
(52) Zhang, Z.; Zeng, Y.; Jiang, C.-S.; Huang, Y.; Liao, M.; Tong, H.; Al-Jassim, M.; Gao, P.; Shou, C.; Zhou, X.; et al. Carrier Transport through the Ultrathin Silicon-Oxide Layer in Tunnel Oxide Passivated Contact (TOPCon) c-Si Solar Cells. *Sol. Energy Mater. Sol. Cells* **2018**, *187*, 113−122.
(53) Marchat, C.; Connolly, J. P.; Kleider, J.-P.; Alvarez, J.; Koduvelikulathu, L. J.; Puel, J. B. KPFM Surface Photovoltage Measurement and Numerical Simulation. *EPJ Photovoltaics* **2019**, *10*, 3.
(54) Miller, E. M.; Kroupa, D. M.; Zhang, J.; Schulz, P.; Marshall, A. R.; Kahn, A.; Lany, S.; Luther, J. M.; Beard, M. C.; Perkins, C. L.; et al. Revisiting the Valence and Conduction Band Size Dependence of PbS Quantum Dot Thin Films. *ACS Nano* **2016**, *10*, 3302−3311.
(55) Niquet, Y. M.; Allan, G.; Delerue, C.; Lannoo, M. Quantum Confinement in Germanium Nanocrystals. *Appl. Phys. Lett.* **2000**, *77*, 1182−1184.
(56) Niquet, Y. M.; Delerue, C.; Allan, G.; Lannoo, M. Method for Tight-Binding Parametrization: Application to Silicon Nanostructures. *Phys. Rev. B: Condens. Matter Mater. Phys.* **2000**, *62*, 5109−5116.
(57) Mélin, T.; Diesinger, H.; Deresmes, D.; Stiévenard, D. Probing Nanoscale Dipole-Dipole Interactions by Electric Force Microscopy. *Phys. Rev. Lett.* **2004**, *92*, 166101.



https://doi.org/10.1021/acs.jpcc.1c02079
*J. Phys. Chem. C* 2021, 125, 12870−12879